Antidisturbance Speed Control for Induction Machine Drives Using High-Order Fast Terminal Sliding-Mode Load Torque Observer

Bo Wang, *Student Member, IEEE*, Cheng Luo, Yong Yu, Gaolin Wang, *Member, IEEE*, and Dianguo Xu, *Fellow, IEEE*

***Abstract*—Speed loop is the key factor affecting the performance of induction machine (IM) drives. Conventionally, the proportional integral (PI) controller is applied for its simple implementation and static-errorless; however, its performance degrades apparently under sudden external load torque changes. To address this problem, this paper presents a nonlinear control strategy, combining the conventional PI control with a high-order fast terminal sliding-mode (HOFTSM) load torque observer. The external load torque is estimated online by the proposed HOFTSM observer, and then the estimated torque is used as feed-forward compensation for the PI controller. Moreover, the designed HOFTSM observer shows superiorities in fast convergence rate and chattering elimination. Comparison experiments show that the load torque rejection of the IM speed loop is significantly enhanced by using the proposed approach.**

***Index Terms*—Chattering elimination, high-order fast terminal sliding-mode (HOFTSM), induction machine (IM) drives, load torque observer, speed loop.**

I. Introduction

SPEED control of induction machine (IM) drives is still expected to exhibit more excellent performance in modern industrial manufacturing [1], [2]. Conventionally, linear control schemes, such as proportional integral (PI) control, are used for speed control owing to the simple idea and facile realization [3]. However, in practical application, the speed control is usually nonlinear and time varying due to the internal disturbance (parameter variation and unmodeled dynamics) and external disturbance (sudden load torque changes) [4]. Among these disturbances, the sudden external load torque changes will inevitably cause speed fluctuation, leading to deteriorated performance of the conventional PI control-based speed loop. Although this speed fluctuation can be ignored in general industrial applications, it is unacceptable in high-precision industrial applications, e.g., computer-numeric controlled (CNC) machine tools.

Different algorithms have been presented in recent years to improve the antidisturbance performance of the speed loop, such as two-degree-of-freedom PI control [5], adaptive control [6], predictive control [2], [7], fuzzy control [8], sliding-mode control (SMC) [9], disturbance observer (DO)-based control [4], [10]–[11], and so on. Among these algorithms, DO-based control is regarded as a kind of optimal approaches with strong antidisturbance ability. The basic idea of DO-based control is first put forward by Ohnishi in 1987 [12]. On this basis, DO-based control has been extensively applied in different industry applications [13]–[17]. In DO-based control, the linear DO is conventionally employed due to its simple structure; however, its dynamic performance and robustness is limited. To solve this problem, the nonlinear DO is considered as a promising approach. In [15], a nonlinear DO is derived to estimate the disturbance of a highly nonlinear and coupled system for robotic manipulator control. Kim [18] presents a fuzzy DO for nonlinear control system, which improves the system stability and tracking accuracy obviously. In [19], the neural network theory is combined with the linear DO to estimate the unknown nonlinear disturbances for motor position control.

For the speed control of AC motor drive, the application of DO-based control has also received increasing attention. As the key technology of DO-based speed control, the load torque estimation is a pivotal issue. In [20] and [21], a kind of extended state observer (ESO) taking the load torque as the extended state is proposed for the speed control of permanent-magnet synchronous motor. However, the presented ESO is essentially a linear DO, and thus its performance degrades under motor and load-side parameter mismatch. Lin *et al*. [22] introduce the conventional SMC into the design of DO to enhance its robustness, but the inherent high-frequency switching control of SMC causes the chattering problem. On this foundation, Zhang *et al*. [23] combine the conventional SMC with ESO to estimate the load torque. Although the estimated torque can be smoothed by applying the low-pass filter structure, the chattering problem still exists in the designed ESO. Milosavljevic *et al*. [24] further propose an integral discrete-time SMC to achieve chattering-free control for servo drives. A parallel connection of first- and

Manuscript received March 9, 2017; revised July 16, 2017 and September 11, 2017; accepted October 12, 2017. Date of publication October 22, 2017; date of current version June 22, 2018. This work was supported in part by the Research Fund for the National Science Foundation of China under Grant 51377032, and in part by the Research Fund for the National Science and Technology Support Program under Grant 2014BAF08B05. Recommended for publication by Associate Editor B. G. Fernandes. *(Corresponding author: Bo Wang.)*

The authors are with the School of Electrical Engineering and Automation, Harbin Institute of Technology, Harbin 150001, China (e-mail: wangbo6222@126.com; c.luo.hit@foxmail.com; yuyong@hit.edu.cn; WGL818@hit.edu.cn; xudiang@hit.edu.cn).

Color versions of one or more of the figures in this paper are available online at http://ieeexplore.ieee.org.

Digital Object Identifier 10.1109/TPEL.2017.2765522

second-order observers is applied for load torque estimation. However, the dynamic performance of the designed observer is limited against sudden load torque changes.

To improve the load-torque rejection of IM speed control, this paper proposes a PI controller with high-order fast terminal sliding-mode (HOFTSM) load torque observer. The proposed HOFTSM-based observer can accurately estimate the system load torque, and then the estimated torque is used as the feed-forward compensation for the PI controller to suppress the speed fluctuations caused by external load torque changes. Moreover, the proposed observer can not only ensure the fast convergence of the estimated load torque, but also eliminate the inherent chattering of the conventional SMC-based observer.

This paper is organized as follows. In Section II, the mathematical model and mechanical dynamics of IM are first given. Then, the rotor field-oriented control (RFOC) [25] is applied as the basic control strategy for IM drive. Section III derives the conventional PI control for IM speed loop in frequency domain. In Section IV, the HOFTSM load torque observer-based control is proposed, following with the analysis of the observer stability and finite-time convergence. In Section V, comparison experiments are performed on an industrial IM drive to validate the proposed algorithm.

II. System Descriptions

A. IM Model

In synchronous rotating d–q reference frame, the RFOC-based IM mathematical model [25] can be expressed as follows:

$$\begin{cases} \dot{i}_{sd} = -\frac{R_s L_r^2 + R_r L_m^2}{\sigma L_s L_r^2} i_{sd} + \omega_e i_{sq} + \frac{L_m}{\sigma L_s L_r T_r} \lambda_r + \frac{u_{sd}}{\sigma L_s} \\ \dot{i}_{sq} = -\frac{R_s L_r^2 + R_r L_m^2}{\sigma L_s L_r^2} i_{sq} - \omega_e i_{sd} - \frac{L_m}{\sigma L_s L_r} \omega_r \lambda_r + \frac{u_{sq}}{\sigma L_s} \end{cases} \tag{1}$$

where i_{sd} and i_{sq} represent stator current $d-q$ components; u_{sd} and u_{sq} represent stator voltage $d-q$ components; λ_r is the rotor flux; R_s and R_r are stator and rotor resistances; L_s, L_r, and L_m are self- and mutual inductances; ω_e is the synchronous angular speed; ω_r is the rotor angular speed; $T_r = L_r / R_r$ is the rotor time constant; and $\sigma = 1 - L_m^2/(L_s L_r)$ is the leakage coefficient.

The IM mechanical dynamics [5] is given by the following:

$$\dot{\omega}_r = \frac{T_e}{J} - \frac{T_L + B\omega_r}{J} = \frac{T_e - T_l}{J} \tag{2}$$

where $T_e = K_t\, i_{sq}$ is electrical magnetic torque; $K_t = n_p\, L_m\, \lambda_r / L_r$; n_p is the number of pole pairs; T_l is the load torque; T_L is torque independent of the speed, B is the viscous friction coefficient; and J is the rotational inertia.

Applying the Laplace transform in (2), the transfer function of IM mechanical dynamics from $T_e - T_l$ to ω_r can be derived as follows:

$$G(s) = \frac{1}{Js}. \tag{3}$$

B. RFOC-Based IM Drive

Fig. 1 shows the block diagram of the RFOC-based IM drive. The overall algorithm employs the commonly used cascade dual closed-loop structure, including speed loop and current loop.

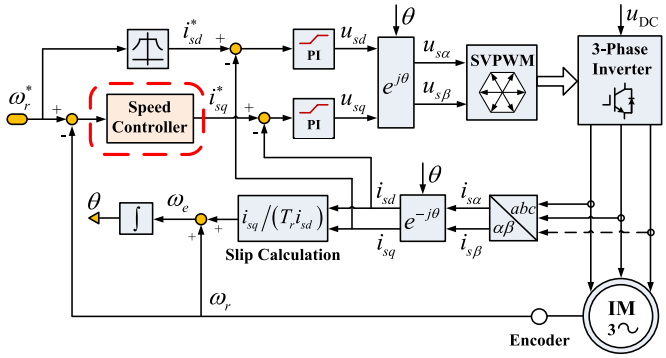

Fig. 1. Block diagram of the RFOC-based IM drive.

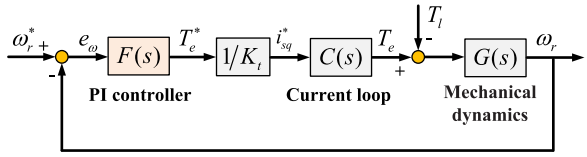

Fig. 2. Simplified diagram of the PI control-based speed loop.

Two PI controllers in the synchronous frame are applied as the current loop regulators. The reference of i_{sd} (represents the field current) remains constant under the rated speed; and the reference of i_{sq} (represents the torque current) varies according to the speed loop output. The rotor position θ used for coordinate transformation is obtained by integrating the synchronous angular speed ω_e. The IM machinery speed is measured by an incremental encoder. In this paper, we focus on the performance improvement of the speed controller.

III. Conventional PI Control-Based Speed Loop and its Limitations

The PI controller is conventionally used as the speed loop regulator for its simple implementation and static-errorless [5]. The transfer function of a standard PI controller is as follows:

$$F(s) = K_p + \frac{K_i}{s} \tag{4}$$

where K_p and K_i are the proportional and integral coefficients, respectively.

The simplified diagram of the PI control-based speed loop is shown in Fig. 2. The reference speed ω_r^* and the measured speed ω_r serve as the system input and output, respectively. By applying the PI control with back electromotive force feedforward compensation in the current loop [25], [26], the current loop transfer function can be expressed as follows:

$$C(s) = \frac{K_t}{T_c s + 1} \tag{5}$$

where $1/T_c$ is the bandwidth of the current loop.

The system open-loop transfer function from ω_r^* to ω_r can be derived as follows:

$$G_o(s) = \frac{1}{K_t} F(s) C(s) G(s) = \left(K_p + \frac{K_i}{s}\right) \frac{1}{Js(T_c s + 1)}. \tag{6}$$

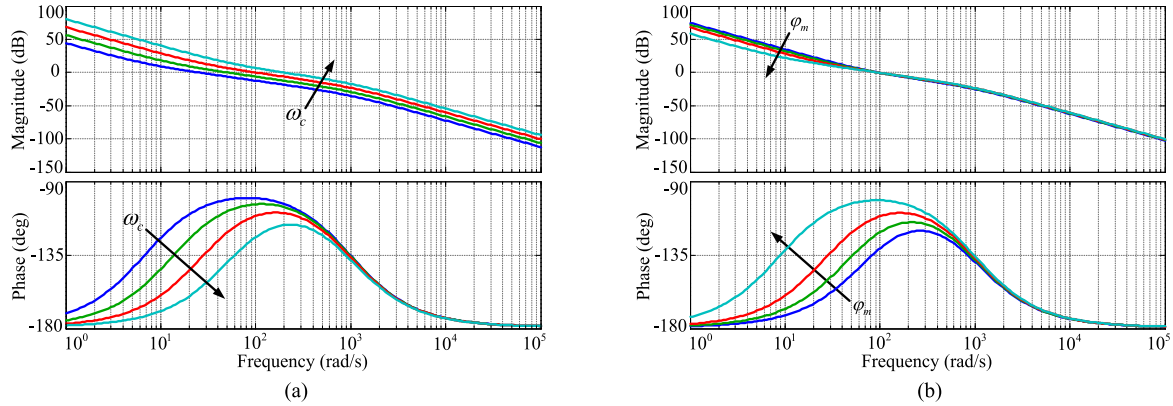

Fig. 3. Bode plots of the PI control-based speed loop. (a) ω_c varied between 50 rad/s and 200 rad/s (step size of 50 rad/s), $\varphi_m = 75°$. (b) φ_m varied between 55° and 85° (step size of 10°), $\omega_c = 100\,\mathrm{rad/s}$.

According to the definition of crossover frequency ω_c and phase margin φ_m [27], we obtain the following:

$$|G_o(j\omega_c)| = \sqrt{K_p^2 + \frac{K_i^2}{\omega_c^2}}\frac{1}{J\omega_c\sqrt{T_c^2\omega_c^2+1}} = 1 \tag{7}$$

$$\varphi_m = \pi + \arg G_o(j\omega_c) = \arctan\frac{K_p\omega_c}{K_i} - \arctan T_c\omega_c. \tag{8}$$

As the system inner loop, the bandwidth of current loop $1/T_c$ is generally much higher than that of the speed loop (outer loop). And, thus, we can get $T_c^2\omega_c^2 \ll 1$. On this basis, the expressions of K_p and K_i can be derived by solving (7) and (8)

$$K_p = J\omega_c \sin\varphi_m \tag{9}$$

$$K_i = J\omega_c^2 \cos\varphi_m. \tag{10}$$

To achieve satisfactory speed loop performance, we need to adjust ω_c and φ_m in (9) and (10). Fig. 3 shows the Bode plots of the PI control-based speed loop with different ω_c and φ_m. The IM parameters used for analysis are shown in the Appendix. The bandwidth of the current loop is set to $1/T_c = 1000$ rad/s.

It can be seen from Fig. 3 (a) that the system cutoff frequency increases with the increase of ω_c, meaning that fast transient response is achieved. However, excessive ω_c will result in small phase margin and large overshoot, causing system performance deterioration, even instability. Besides, the inner loop (current loop) bandwidth further limits the maximum value of ω_c. In Fig. 3(b), the phase margin increases as the increase of φ_m, leading to enhanced system stability. But likewise, excessive φ_m will result in long settling time. Therefore, the selection of ω_c and φ_m should be a tradeoff between system rapidity and stability.

Let us further discuss the load-torque rejection of PI control-based speed loop. According to Fig. 2, the error transfer function from T_l to e_ω can be derived as follows:

$$G_l(s) = \frac{G(s)}{1 + F(s)C(s)G(s)/K_t} = \frac{T_c s^2 + s}{T_c J s^3 + J s^2 + K_p s + K_i}. \tag{11}$$

As depicts in [27], the integrated error (IE) can be used to measure the load-torque rejection performance. When a load-torque step ΔT_l is applied, the IE of the speed loop can be described as follows:

$$\mathrm{IE} = \int_0^\infty e_\omega\,dt = L\{e_\omega\}_{s=0} = \lim_{s\to 0} G_l(s)\frac{\Delta T_l}{s} = \frac{\Delta T_l}{K_i} = \frac{\Delta T_l}{J\omega_c^2\cos\varphi_m} \tag{12}$$

where "L" represents the Laplace transform.

To obtain strong load-torque rejection, IE should be selected as small as possible, meaning that we need to choose large ω_c and small φ_m. However, as analyzed hereinbefore, excessive ω_c will result in system overshoot, even instability, and too small φ_m will reduce the system stability margin. Therefore, the load-torque rejection of PI control-based speed loop is limited due to the contradiction between system rapidity and stability. And this limitation will exercise a significant adverse impact on high-precision applications, such as CNC machine tools.

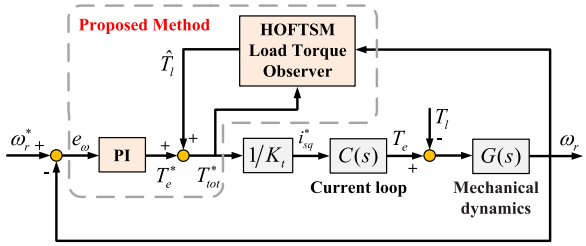

Fig. 4. Block diagram of the proposed HOFTSM load torque observer-based controller for the IM speed loop.

IV. Proposed HOFTSM Load Torque Observer-Based Control

To improve load-torque rejection of the IM speed loop, a HOFTSM load torque observer-based control is proposed as shown in Fig. 4. Unlike the conventional single PI control (see Fig. 2), the system load torque is estimated online, and then applied as feed-forward compensation for the PI control. If the estimated load torque can converge to its real value in finite sampling periods, the load torque reference contributed by PI control can be canceled, leading to an exact linearization of control system. The output T_{tot}^* of the proposed controller is

designed as follows:

$$T_{\text{tot}}^{*} = T_e^{*} + \hat{T}_l \tag{13}$$

where $T_e^{*} = K_p e_\omega + K_i \int e_\omega dt$ is the torque reference contributed by the PI control and $\hat{T}_l$ is the estimated load torque.

In this section, the principle and advantages of the HOFTSM technique is first introduced. And then the HOFTSM technique is used for the design of load torque observer.

A. Principle and Advantages of HOFTSM

Compared with the linear control (e.g., PI control), SMC is well known for its fast global convergence and strong robustness to system disturbance. And it has been successfully applied in many industry applications [28]. Generally, the design of SMC involves two steps: 1) a sliding-mode surface, which plans the trajectory of system dynamics, is selected for desired performance; 2) the control law is designed to force system dynamics to reach sliding-mode surface and stay on it thereafter.

Consider an uncertain nonlinear system

$$\dot{x} = f(x) + d(x) + u \tag{14}$$

where $x \in R^n$ is the state variable; $u \in R$ is the control input; $f(x)$ is the uncertain smooth function of x; and $d(x)$ represents the system disturbance. For clarity, only single input single output system is considered here.

As depicted in [29], terminal sliding-mode (TSM) surface and fast terminal sliding-mode (FTSM) surface can be described by the following equation:

$$s = \dot{x} + \beta |x|^{\gamma} \operatorname{sign}(x) = 0 \tag{15}$$

$$s = \dot{x} + \alpha x + \beta |x|^{\gamma} \operatorname{sign}(x) = 0 \tag{16}$$

where α, $\beta > 0$, and $0 < \gamma < 1$ are constants. Compared with the conventional linear sliding-mode surface, the presented nonlinear surfaces, especially the FTSM surface (16), show superiorities in convergence rate and steady-state tracking accuracy [29].

As for the design of control law, the first-order SMC is conventionally applied; however, it suffers from the chattering problem due to its essential high-frequency switching control. The chattering is highly undesirable since it will cause high-frequency oscillations and control accuracy degradation. The recent research works of chattering elimination can be mainly divided into three categories. The first category is the boundary layer method [30]. The sign function of conventional SMC is replaced by a sigmoid-like function or a saturation function within the layer. However, this kind of approach is at the price of system robustness. The second category is applying an additional low-pass filter to smooth the switching control signal, but it will introduce the phase lag at the same time [31]. The third category is the high-order sliding-mode (HOSM) method [32]. By shifting the discontinuous control to the derivative of control law, the HOSM achieves chattering-free control in theory. As an extension, the stability and robustness of HOSM using a TSM surface has been proved in [33].

In this paper, the HOFTSM is presented combining the HOSM with an FTSM surface. The simplest form of the control law can be given by the following:

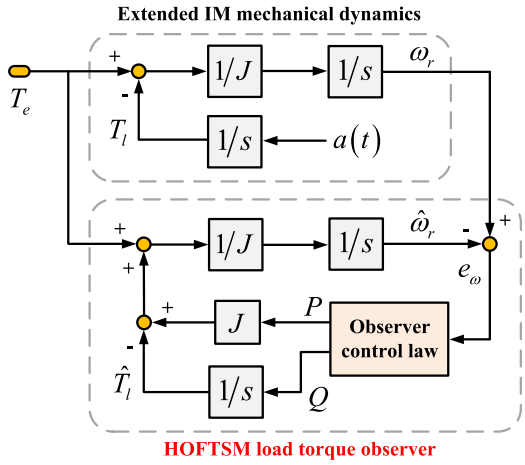

Fig. 5. Block diagram of the proposed HOFTSM load torque observer.

$$u = -f(x) - \beta |x|^{\gamma} \operatorname{sign}(x) + u_n \tag{17}$$

$$\dot{u}_n + T u_n = -k \operatorname{sign}(s) \tag{18}$$

where s is given by (16); $u_n(0) = 0$; and T, $k > 0$ are the designed parameters. By selecting T and k appropriately, the controller is robustly stable to the system disturbances $d(x)$.

In brief, the advantages of the presented HOFTSM are as following:

1) it maintains the fast convergence and strong robustness of the conventional SMC;
2) it shows strengths in finite-time convergence and steady-state tracking accuracy by using the FTSM surface;
3) it essentially eliminates the chattering problem of the conventional SMC by applying the HOSM.

B. HOFTSM Load Torque Observer

In (2), regarding T_l as the system extended state [20], [21], the extended IM mechanical dynamics can be expressed as follows:

$$\begin{cases} \dot{\omega}_r = \frac{T_e}{J} - \frac{T_l}{J} \\ \dot{T}_l = a \end{cases} \tag{19}$$

where a is the derivative of the load torque T_l.

Then, the HOFTSM load torque observer is designed as follows:

$$\begin{cases} \dot{\hat{\omega}}_r = \frac{T_e}{J} - \frac{\hat{T}_l}{J} + P \\ \dot{\hat{T}}_l = Q \end{cases} \tag{20}$$

where $\hat{}$ represents the estimated value; P is the designed control law; and Q is the designed equivalent load torque derivative. Fig. 5 shows the block diagram of the proposed HOFTSM load torque observer.

By subtracting (20) from (19), we can obtain the system error state equation as follows:

$$\begin{cases} \dot{e}_\omega = -\frac{e_T}{J} - P \\ \dot{e}_T = a - Q \end{cases} \tag{21}$$

where $e_\omega = \omega_r - \hat{\omega}_r$ is the speed estimated error; and $e_T = T_l - \hat{T}_l$ is the load torque estimated error.

According to (16), a FTSM surface is designed to achieve finite-time convergence and better tracking accuracy

$$s = \dot{e}_\omega + \alpha e_\omega + \beta |e_\omega|^\gamma \text{sign}(e_\omega) = 0 \tag{22}$$

where α, β, and γ are constants defined as (16).

Theorem 1: For the error system (21), the FTSM surface (22) will be reached, and the states e_ω and $\dot{e}_\omega$ can converge to 0 along the FTSM surface within finite time, if the HOSM control law is designed as follows:

$$P = \alpha e_\omega + \beta |e_\omega|^\gamma \text{sign}(e_\omega) + P_n \tag{23}$$

$$\dot{P}_n + \omega_f P_n = k_1 \text{sign}(s) \tag{24}$$

where $P_n(0) = 0$; and ω_f, k_1 are the designed parameters of the control law. And the equivalent load torque derivative is designed as follows:

$$Q = -k_2 \text{ sign}(s) \tag{25}$$

where k_2 is the designed parameter.

Proof: Consider a Lyapunov function $V = s^2/2$. Then, its derivative with respect to time t can be given by the following:

$$\dot{V} = s\dot{s}. \tag{26}$$

The sliding-mode surface s can be rewritten by substituting the first equation of (21) into (22) as follows:

$$s = -\frac{e_T}{J} - P + \alpha e_\omega + \beta |e_\omega|^\gamma \text{sign}(e_\omega). \tag{27}$$

By substituting (23) into (27), we obtain the following:

$$\begin{aligned} s &= -\frac{e_T}{J} - \alpha e_\omega - \beta |e_\omega|^\gamma \text{sign}(e_\omega) \\ &\quad - P_n + \alpha e_\omega + \beta |e_\omega|^\gamma \text{sign}(e_\omega) = -\frac{e_T}{J} - P_n. \end{aligned} \tag{28}$$

Then, the derivative of s with respect to time t can be expressed as follows:

$$\dot{s} = -\frac{\dot{e}_T}{J} - \dot{P}_n. \tag{29}$$

Substituting the second equation of (21) and (24) into (29) yields the following:

$$\dot{s} = -\frac{a - Q}{J} - k_1 \text{sign}(s) + \omega_f P_n. \tag{30}$$

Further substituting (25) into (30), we obtain the following:

$$\begin{aligned} \dot{s} &= -\frac{a - (-k_2 \text{sign}(s))}{J} - k_1 \text{sign}(s) + \omega_f P_n \\ &= -\left(k_1 + \frac{k_2}{J}\right) \text{sign}(s) + \omega_f P_n - \frac{a}{J}. \end{aligned} \tag{31}$$

Thus, $\dot{V}$ can be rewritten by substituting (31) into (26) as follows:

$$\begin{aligned} s\dot{s} &= s\left(-\left(k_1 + \frac{k_2}{J}\right) \text{sign}(s) + \omega_f P_n - \frac{a}{J}\right) \\ &= -\left(k_1 + \frac{k_2}{J}\right)|s| + \omega_f P_n s - \frac{as}{J} \\ &= (-k_1 |s| + \omega_f P_n s) + \left(\frac{-k_2 |s| - as}{J}\right). \end{aligned} \tag{32}$$

By selecting $k_1 > |\omega_f P_n|$, $k_2 > |a| + \eta J$, and η is a positive constant, we obtain the following:

$$\dot{V} = s\dot{s} < -\eta |s| < 0 \quad \text{for} \quad s \neq 0. \tag{33}$$

Therefore, on the basis of the Lyapunov stability theorem, the system dynamics can converge to the FTSM surface (22) within finite time, and stay on it thereafter. Then, we can obtain $s = 0$, and the system dynamics is determined by the following nonlinear differential equation:

$$\dot{e}_\omega + \alpha e_\omega + \beta |e_\omega|^\gamma \text{sign}(e_\omega) = 0. \tag{34}$$

According to the finite-time stability theorem [34], given an initial condition $e_\omega(0) \neq 0$, e_ω can converge to 0 within finite time with properly chosen α, β, and γ. Its physical interpretation can be expressed as follows: when the system dynamics is far away from $e_\omega = 0$, (34) can be approximated as $\dot{e}_\omega = -\alpha e_\omega$, meaning that the convergence rate is fast; when close to $e_\omega = 0$, (34) is approximated as $\dot{e}_\omega = -\beta |e_\omega|^\gamma sign(e_\omega)$ which is a terminal attractor [35]. By solving the differential equation (34) analytically, the exact time to reach $e_\omega = 0$ can be calculated as follows:

$$t_s = \frac{1}{\alpha(1-\gamma)} \ln \frac{\alpha |e_\omega(0)|^{1-\gamma} + \beta}{\beta}. \tag{35}$$

Furthermore, by substituting $e_\omega = 0$ into (34), we obtain the following:

$$e_\omega = \dot{e}_\omega = 0. \tag{36}$$

Therefore, the proposed approach can provide HOSM (as defined in [32]).

In conclusion, the FTSM surface can be reached within finite-time first, and then the finite-time convergence of the states e_ω and $\dot{e}_\omega$ to 0 is ensured by applying the FTSM surface. This completes the proof.

Remark 1: Convergence of e_T: By applying $s = 0$ in (24), P_n can be derived as follows:

$$P_n = Ce^{-\omega_f t}. \tag{37}$$

Then, substituting (37) and $s = 0$ into (28), we can obtain the expression of e_T as follows:

$$e_T = Js - JP_n = -JCe^{-\omega_f t}. \tag{38}$$

To guarantee the convergence of the load torque estimation error e_T, the control parameter should be selected as $\omega_f > 0$. And the convergence rate of e_T can be optimized by adjusting ω_f.

Remark 2: Calculation of Sign(s): It can be seen from (23) to (25) that the value of $\mathrm{sign}(s)$ is crucial for the control law. However, the variable $\dot{e}_\omega$ in s [see (22)] is unavailable, so $\mathrm{sign}(s)$ cannot be obtained directly. Note that we only need the sign of s, not the value of s. According to this idea and the discrete control property, we can rewrite $\mathrm{sign}(s)$ as follows:

$$\mathrm{sign}\,(s) = \mathrm{sign}\left(\lim_{T_s \to 0} \frac{b\,(t+T_s) - b\,(t)}{T_s}\right) \tag{39}$$

where T_s is the sampling period of the control loop; and $b(t)$ is the integral of $s(t)$, which can be calculated by integrating (22)

$$b\,(t) = \int_0^t s\,(t)\,dt = e_\omega + \int_0^t \left(\alpha e_\omega + \beta |e_\omega|^\gamma\ \mathrm{sign}\,(e_\omega)\right) dt.$$

Since $T_s > 0$, we can rewrite (39) as follows:

$$\mathrm{sign}\,(s) = \mathrm{sign}\,(b\,(t+T_s) - b\,(t))\,. \tag{40}$$

Thus, $\mathrm{sign}(s)$ can be tactfully calculated by using (40) without $\dot{e}_\omega$.

Remark 3: Chattering Suppression Analysis: The chattering suppression of the proposed HOFTSM load torque observer is analyzed. According to the second equation of (20), we obtain the following:

$$\hat{T}_l = \int Q dt. \tag{41}$$

Thus, the proposed observer can output the smoothed estimated load torque $\hat{T}_l$ by integrating chattering signal Q [see (25)].

As for the control law P, it can be seen from (23) and (24) that the chattering signal $k_1 \mathrm{sign}(s)$ in P is smoothed by an equivalent low-pass filter. According to (24), the transfer function of this low-pass filter from $k_1 \mathrm{sign}(s)$ to P_n can be derived as follows:

$$G_f(s) = \frac{1}{s + \omega_f} \tag{42}$$

where ω_f is the bandwidth of the low-pass filter. Therefore, the proposed observer possesses smooth control law as well.

V. Experimental Results

A. Experimental Setup

To validate the proposed algorithm, an IM drive prototype has been built in the laboratory, as shown in Fig. 6. Two IMs of the same model and rating are connected via a flexible coupling (see Fig. 7). One is applied to test the algorithm, and the other one is used to provide the load torque. The IM parameters are listed in the Appendix. A rectifier and inverter set is applied to drive the test IM. An industrial incremental encoder with the resolution of 1024 P/R is used to measure the IM mechanical speed. A TMS320F28335 Texas Instruments DSP executes the proposed algorithm through a linked computer. The adopted DSP is a 32-bit fixed-point microcontroller with 150 MHz of clock frequency. Two phase currents are measured using the sampling resistances. The SVPWM with 8 kHz switching frequency is applied to generate the switching signal for the inverter. The sampling period of the control loop is 125 μs.

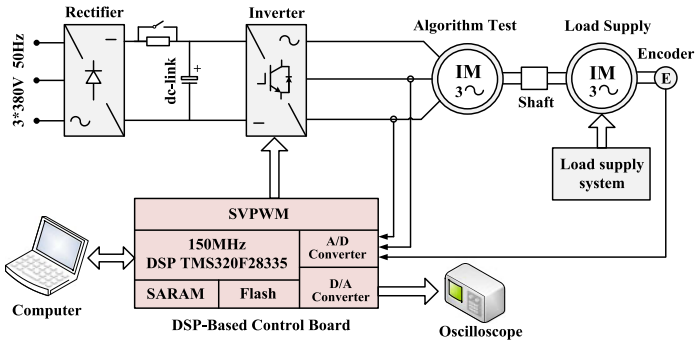

Fig. 6. Block diagram of the laboratory prototype.

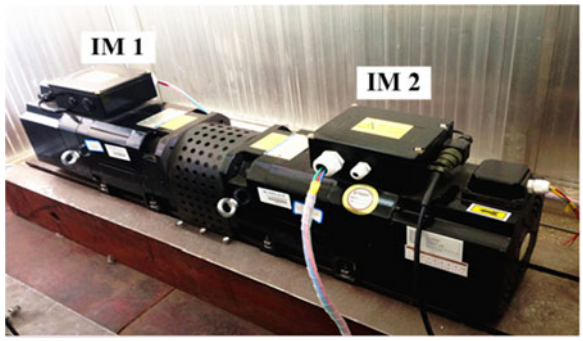

Fig. 7. Photograph of the IMs.

The RFOC (see Fig. 1) is applied as the basic control algorithm. The reference of i_{sd} and the saturation limit of i_{sq} are set to 6.0 A and 12.6 A via the synchronous rotation coordination transformation, respectively. The bandwidth of the two current loops is set to 1000 rad/s. The parameters of the designed HOFTSM load torque observer are $\alpha = 1$; $\beta = 2$; $\gamma = 1/2$; $\omega_f = 100$; $k_1 = 50$; and $k_2 = 200$.

B. Experimental Results With the Conventional PI Controller

Figs. 8 and 9 give the experimental results of the conventional PI controller against speed step change and sudden load torque changes under different control parameters. The waveforms of machine speed ω_r and its reference ω_r^*, and the q-axis current i_{sq} (represents the torque current) are given per figure.

In Fig. 8, the crossover frequency ω_c is selected as 40, 70, and 100 rad/s, respectively, and the phase margin φ_m is fixed as 75°. As ω_c increases, the rise time against speed step change reduces (see Fig. 8 (a)), and the load torque rejection is strengthened [see Figs. 8(b) and (c)]. Nevertheless, it does not mean that the speed loop performance can be unlimited improved by increasing ω_c. As analyzed in Section III, the maximum value of ω_c is limited by control overshoot and restriction of the inner loop (current loop) bandwidth.

In Fig. 9, the crossover frequency ω_c is fixed as 100 rad/s, and the phase margin φ_m is selected as 65°, 75°, and 85°, respectively. The overshoot against speed step change is reduced by increasing φ_m. However, overlarge φ_m leads to long rise time

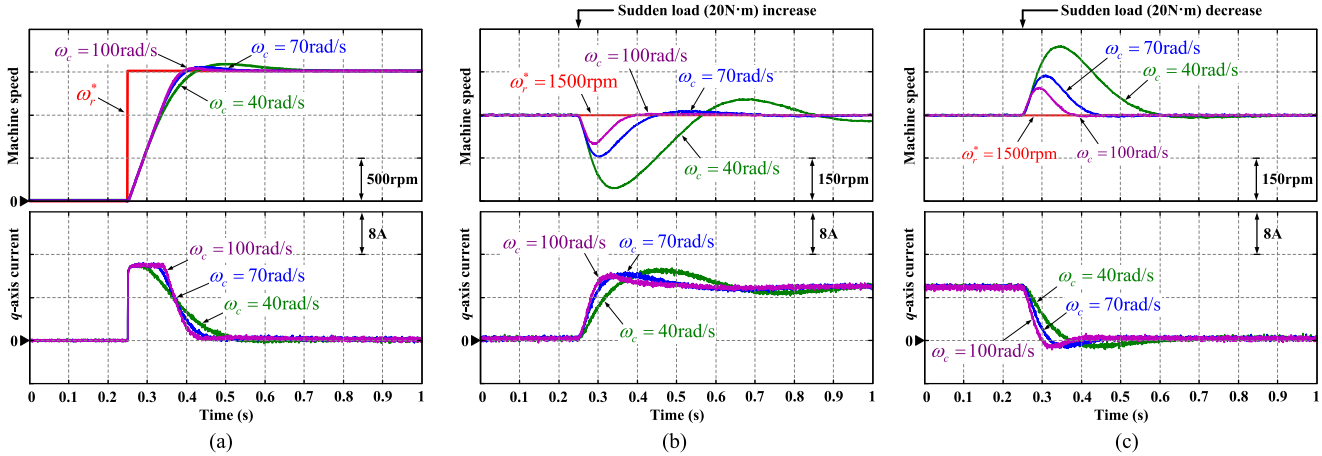

Fig. 8. Experimental results of the PI controller with different ω_c. (a) Step speed change. (b) Sudden load torque (20 N·m) increase. (c) Sudden load torque (20 N·m) decrease.

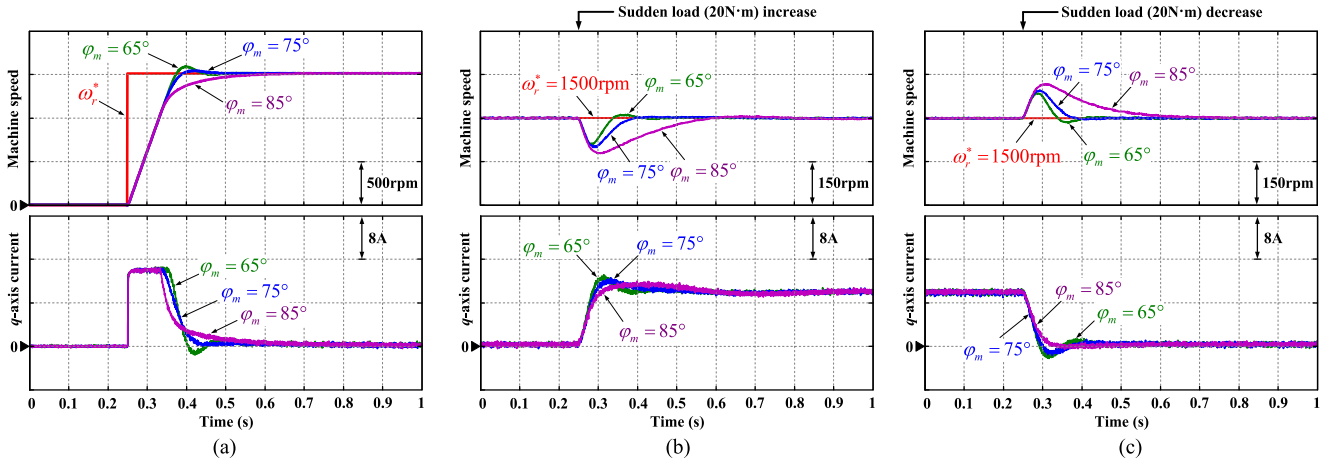

Fig. 9. Experimental results of the PI controller with different φ_m. (a) Step speed change. (b) Sudden load torque (20 N·m) increase. (c) Sudden load torque (20 N·m) decrease.

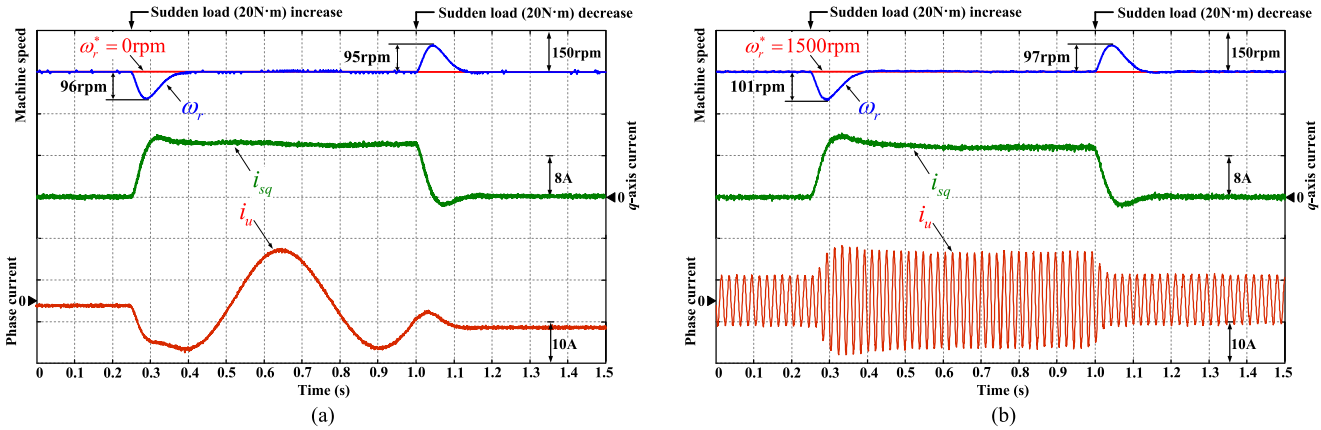

Fig. 10. Experimental results of the conventional PI controller under sudden load (20 N·m) change. (a) Zero speed (0 r/min). (b) Rated speed (1500 r/min).

[see Fig. 9(a)] and degraded load torque rejection [see Fig. 9(b) and (c)].

Therefore, it is difficult for the conventional PI controller to achieve satisfactory load torque rejection, while maintaining the good step reference tracking.

C. Experimental Results With the Proposed HOFTSM Load Torque Observer-Based Controller

Figs. 10–12 show the experimental results of different schemes under sudden load (20 N·m) changes, respectively.

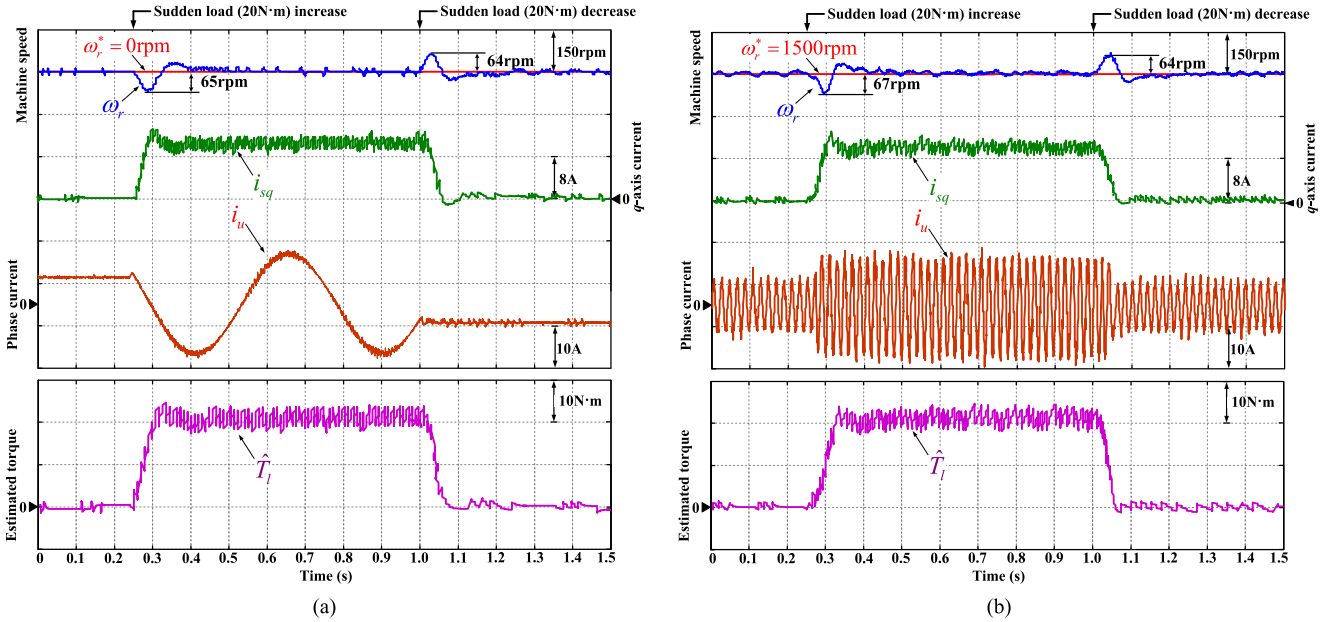

Fig. 11. Experimental results of the conventional SMC load torque observer-based controller under sudden load (20 N·m) change. (a) Zero speed (0 r/min). (b) Rated speed (1500 r/min).

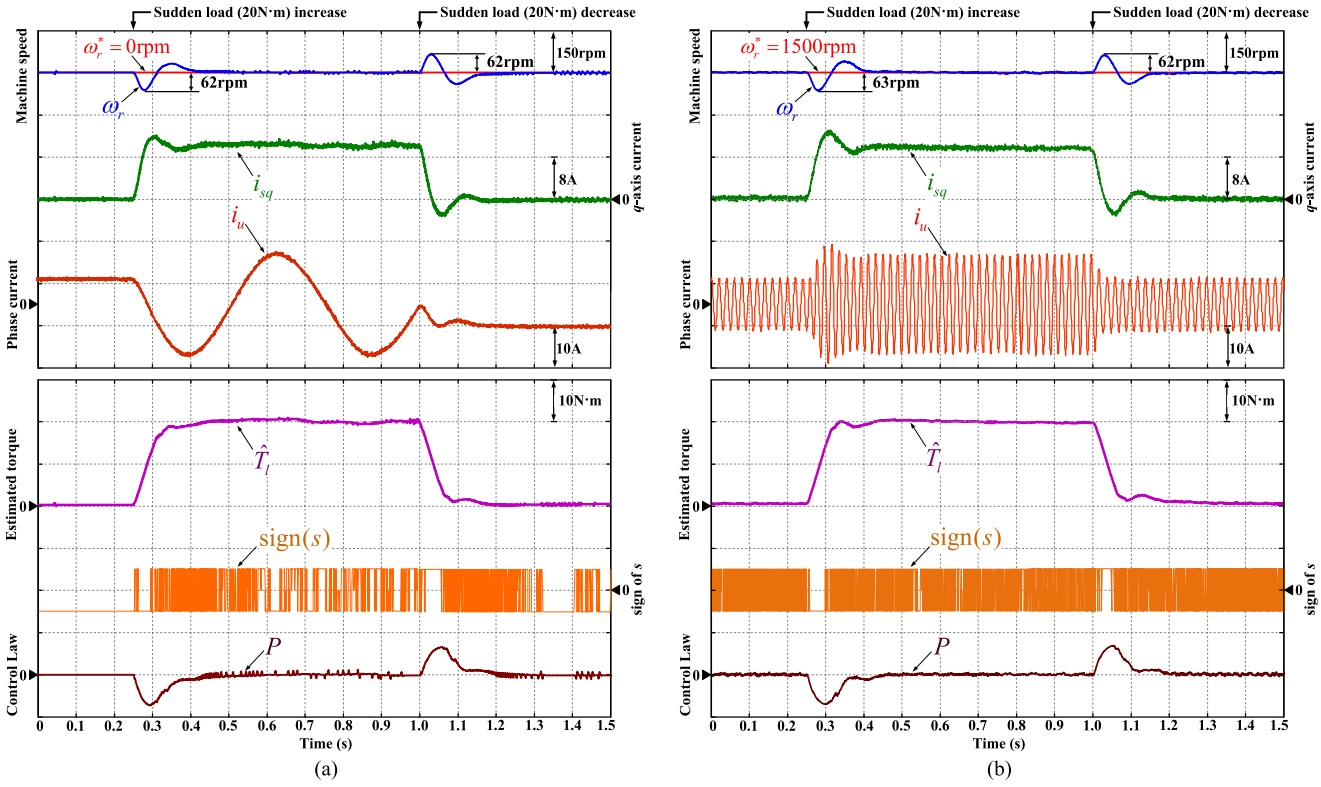

Fig. 12. Experimental results of the proposed HOFTSM load torque observer-based controller under sudden load (20 N·m) change. (a) Zero speed (0 r/min). (b) Rated speed (1500 r/min).

In Figs. 10(a), 11(a), and 12(a), the machine reference speed is set to 0, while it is set to 1500 r/min (rated speed) in Figs. 10(b), 11(b), and 12(b). The parameters of the PI controller are selected as $\omega_c = 100\,\mathrm{rad/s}$ and $\varphi_m = 75°$.

In Fig. 10, the maximum speed fluctuations of the conventional PI controller caused by sudden load changes are 96 r/min (when $\omega_r^* = 0$) and 101 r/min (when $\omega_r^* = 1500$ r/min), respectively. By contrast in Fig. 11, the maximum speed fluctuations

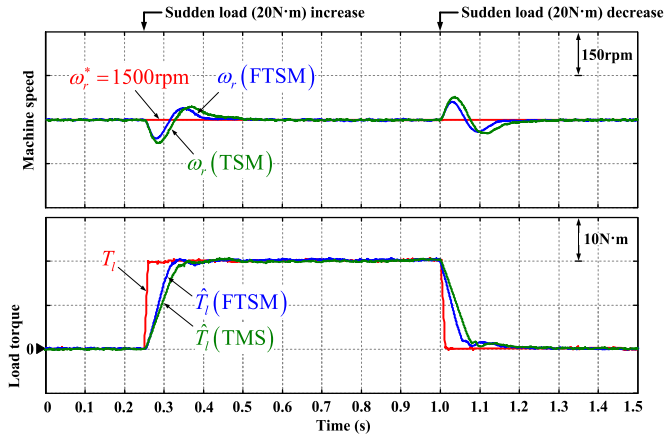

Fig. 13. Comparative experimental results between the proposed FTSM-based controller and TSM-based controller under sudden load (20 N·m) change.

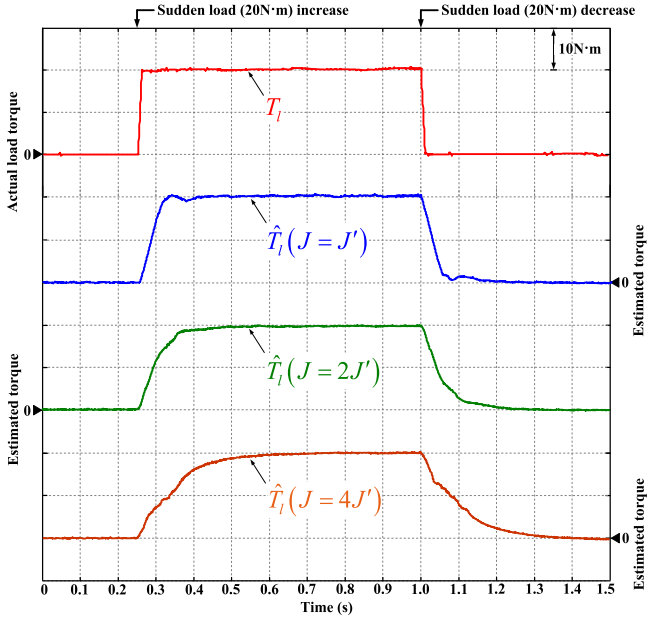

Fig. 14. Estimated torque of the proposed HOFTSM load torque observer under different initial value of *J*.

of the conventional SMC load torque observer-based controller are 65 and 67 r/min, meaning that the load torque rejection of speed loop is improved significantly. However, due to the inherent chattering problem of the conventional SMC, the estimated torque contains lots of high-frequency noise, which degrades the system performance severely.

As shown in Fig. 12, the maximum speed fluctuations of the proposed scheme under the same condition are 62 and 63 r/min. Therefore, compared with the approaches in Figs. 10 and 11, the proposed scheme can achieve the optimal load torque rejection of speed loop. Unlike the conventional SMC load torque observer, the proposed observer can smoothly estimate the load torque. The sign of the sliding-mode surface $\mathrm{sign}(s)$ is high-frequency switching signal, while the control law P is smooth signal. This is in accordance with the theoretical analysis in Section IV. Based on (23), (24), and (42), the chattering signal $\mathrm{sign}(s)$ is not directly used as the control law, but smoothed by an equivalent low-pass filter. Then this smoothed signal is applied as the control law, which indicates that the proposed HOFTSM load torque observer is chattering-free.

To verify the fast convergence performance of the proposed controller, Fig. 13 gives the comparative experimental results between the proposed FTSM-based controller and TSM-based controller under sudden load (20 N·m) change. It can be seen that both controllers can realize accurate speed tracking and load torque observation. However, the convergence rate of the proposed FTSM-based controller is faster than that of the TSM-based controller, which is consistent with the theoretical analysis as shown in Section IV-A.

Furthermore, to evaluate the robustness of the proposed HOFTSM load torque observer, Fig. 14 depicts the experimental result of the proposed observer under system parameter variation. As the major disturbance, the rotational inertia *J* is selected as the tested parameter here [22], and the initial value of J is set to J', $2J'$, and $4J'$, respectively (J' represents the nominal value of rotational inertia). The estimated torque can converge to the actual load torque under different initial value of *J*, meaning that the proposed observer is robust to system parameter variation. However, the convergence time of the estimated torque increases as the error of the initial value of *J* increases.

VI. Conclusion

To enhance the load torque rejection of IM drives, this paper proposes an HOFTSM load torque observer-based controller. Although the performance of the speed loop can be improved by applying a well-tuned PI controller in a certain extent, its load torque rejection ability is still limited. To address this problem, the proposed controller applies the idea of DO-based control, where the load torque is estimated by the proposed HOFTSM observer, and then the estimated torque is applied as the controller feed-forward compensation. This paper also concludes that the proposed HOFTSM observer can not only smoothly estimate the load torque, but effectively eliminate the inherent chattering of SMC. The experimental results performed on an industrial IM drive validate the proposed approach.

Appendix

TABLE I
Parameters of the Induction Machine

Symbol	Quantity	Value
P_N	Rated power	3.7 kW
V_N	Rated voltage	380 V
ω_N	Rated speed	1500 r/min
n_p	Number of pole pairs	2
R_s	Stator resistance	1.142 Ω
R_r	Rotor resistance	0.825 Ω
L_m	Mutual inductance	118.9 mH
L_s, L_r	Stator, rotor inductance	124.4 mH
J_{tot}	Total inertia	$0.0256\,\mathrm{kg}\cdot\mathrm{m}^2$

REFERENCES

[1] L. Amezquita-Brooks, J. Liceaga-Castro, and E. Liceaga-Castro, "Speed and position controllers using indirect field-oriented control: A classical control approach," *IEEE Trans. Ind. Electron.*, vol. 61, no. 4, pp. 1928–1943, Apr. 2014.

[2] Z. Hu and K. Hameyer, "A method of constraint handling for speed-controlled induction machines," *IEEE Trans. Ind. Electron.*, vol. 63, no. 7, pp. 4061–4072, May 2016.

[3] L. Niu, D. Xu, M. Yang, X. Gui, and Z. Liu, "On-line inertia identification algorithm for PI parameters optimization in speed loop," *IEEE Trans. Power Electron.*, vol. 30, no. 2, pp. 849–859, Feb. 2015.

[4] J. Li, H. Ren, and Y. Zhong, "Robust speed control of induction motor drives using first-order auto-disturbance rejection controllers," *IEEE Trans. Ind. Appl.*, vol. 51, no. 1, pp. 712–720, Jan./Feb. 2015.

[5] L. Harnefors, S. Saarakkala, and M. Hinkkanen, "Speed control of electrical drives using classical control methods," *IEEE Trans. Ind. Appl.*, vol. 49, no. 2, pp. 889–898, Mar./Apr. 2013.

[6] J. W. Jung, V. Q. Leu, T. D. Do, E. K. Kim, and H. H. Choi, "Adaptive PID speed control design for permanent magnet synchronous motor drives," *IEEE Trans. Power Electron.*, vol. 30, no. 2, pp. 900–908, Feb. 2015.

[7] C. Wang, M. Yang, W. Zheng, J. Long, and D. Xu, "Vibration suppression with shaft torque limitation using explicit MPC-PI switching control in elastic drive systems," *IEEE Trans. Ind. Electron.*, vol. 62, no. 11, pp. 6855–6867, Nov. 2015.

[8] M. Masiala, B. Vafakhah, J. Salmon, and A. M. Knight, "Fuzzy self-tuning speed control of an indirect field-oriented control induction motor drive," *IEEE Trans. Ind. Appl.*, vol. 44, no. 6, pp. 1732–1740, Nov./Dec. 2008.

[9] S. Li, M. Zhou, and X. Yu, "Design and implementation of terminal sliding mode control method for PMSM speed regulation system," *IEEE Trans. Ind. Informat.*, vol. 9, no. 4, pp. 1879–1891, Nov. 2013.

[10] J. Back and H. Shim, "Adding robustness to nominal output-feedback controllers for uncertain nonlinear systems: A nonlinear version of disturbance observer," *Automatica*, vol. 44, no. 10, pp. 2528–2537, Oct. 2008.

[11] W. Chen, J. Yang, L. Guo, and S. Li, "Disturbance-observer-based control and related methods—An overview," *IEEE Trans. Ind. Electron.*, vol. 63, no. 2, pp. 1083–1095, Feb. 2016.

[12] K. Ohnishi, "A new servo method in mechatronics," *Trans. Jpn. Soc. Elect. Eng.*, vol. 107-D, pp. 83–86, 1987.

[13] W. Kim, D. Shin, D. Won, and C. C. Chung, "Disturbance-observer based position tracking controller in the presence of biased sinusoidal disturbance for electrohydraulic actuators," *IEEE Trans. Control Syst. Technol.*, vol. 21, no. 6, pp. 2290–2298, Nov. 2013.

[14] C. S. Wang, X. L. Li, L. Guo, and Y. W. Li, "A nonlinear-disturbance observer-based DC-bus voltage control for a hybrid AC/DC microgrid," *IEEE Trans. Power Electron.*, vol. 29, no. 11, pp. 6162–6177, Nov. 2014.

[15] Z. Li, C.-Y. Su, L. Wang, Z. Chen, and T. Chai, "Nonlinear disturbance observer based control design for a robotic exoskeleton incorporating fuzzy approximation," *IEEE Trans. Ind. Electron.*, vol. 62, no. 9, pp. 5763–5775, Sep. 2015.

[16] N. Kobayashi, F. P. Wijaya, K. Kondo, and O. Yamazaki, "Induction motor speed-sensorless vector control using mechanical simulator and disturbance torque compensation," *IEEE Trans. Ind. Appl.*, vol. 52, no. 3, pp. 2323–2331, May/Jun. 2016.

[17] H. Chu, B. Gao, W. Gu, and H. Chen, "Low speed control for permanent magnet dc torque motor using observer-based nonlinear triple-step controller," *IEEE Trans. Ind. Electron.*, vol. 64, no. 4, pp. 3286–3296, Apr. 2017.

[18] E. Kim, "A fuzzy disturbance observer and its application to control," *IEEE Trans. Fuzzy Syst.*, vol. 10, no. 1, pp. 77–85, Feb. 2002.

[19] J.-S. Ko and B.-M. Han, "Precision position control of PMSM using neural network disturbance observer on forced nominal plant," in *Proc. IEEE Int. Conf. Mechatronics*, 2006, pp. 316–320.

[20] S. Li and Z. Liu, "Adaptive speed control for permanent-magnet synchronous motor system with variations of load inertia," *IEEE Trans. Ind. Electron.*, vol. 56, no. 8, pp. 3050–3059, Aug. 2009.

[21] H. Liu and S. Li, "Speed control for PMSM servo system using predictive functional control and extended state observer," *IEEE Trans. Ind. Electron.*, vol. 59, no. 2, pp. 1171–1183, Feb. 2012.

[22] S. Lin, Y. Cai, B. Yang, and W. Zhang, "Electrical line-shafting control for motor speed synchronisation using sliding mode controller and disturbance observer," *IET Control Theory Appl.*, vol. 11, no. 2, pp. 205–212, 2017.

[23] X. Zhang, L. Sun, K. Zhao, and L. Sun, "Nonlinear speed control for PMSM system using sliding-mode control and disturbance compensation techniques," *IEEE Trans. Power Electron.,* vol. 28, no. 3, pp. 1358–1365, Mar. 2013.

[24] C. Milosavljevic, B. P. Drazenovic, and B. Veselic, "Discrete-time velocity servo system design using sliding mode control approach with disturbance compensation," *IEEE Trans. Ind. Informat.*, vol. 9, no. 2, pp. 920–927, May 2013.

[25] S. K. Sul, *Control of Electric Machine Drive Systems*. Hoboken, NJ, USA: Wiley, 2011, ch. 5.

[26] A. G. Yepes, A. Vidal, O. Lopez, and J. Doval-Gandoy, "Evaluation of techniques for cross-coupling decoupling between orthogonal axes in double synchronous reference frame current control," *IEEE Trans. Ind. Electron.*, vol. 61, no. 7, pp. 3527–3531, Jul. 2014.

[27] K. Åström and T. Hägglund, *PID Controllers: Theory, Design, and Tuning*, 2nd ed. Research Triangle Park, NC, USA: Instrum. Soc. Amer., 1995.

[28] V. Utkin, *Sliding Modes in Control Optimization*. Berlin, Germany: Springer-Verlag, 1992.

[29] S. Yu, X. H. Yu, and B. Shirinzadehc, "Continuous finite-time control for robotic manipulators with terminal sliding mode," *Automatica*, vol. 41, no. 11, pp. 1957–1964, Nov. 2005.

[30] M.-S. Chen, Y.-R. Hwang, and M. Tomizuka, "A state-dependent boundary layer design for sliding mode control," *IEEE Trans. Automat. Control*, vol. 47, no. 10, pp. 1677–1681, Oct. 2002.

[31] K. L. Kang, J. M. Kim, K. B. Hwang, and K. H. Kim, "Sensorless control of PMSM in high speed range with iterative sliding mode observer," in *Proc. 19th Annu. IEEE Appl. Power Electron. Conf. Expo.*, Feb. 2004, vol. 2, pp. 1111–1116.

[32] A. Levant, "Higher-order sliding modes, differentiation and output- feedback control," *Int. J. Control*, vol. 76, nos. 9/10, pp. 924–941, 2003.

[33] Y. Feng, F. Han, and X. Yu, "Chattering free full-order sliding-mode control," *Automatica*, vol. 50, no. 4, pp. 1310–1314, Apr. 2014.

[34] Y. Hong, J. Huang, and Y. Xu, "On an output finite-time stabilization problem," *IEEE Trans. Automat. Control*, vol. 46, no. 2, pp. 305–309, Feb. 2001.

[35] X. Yu and Z. Man, "Fast terminal sliding mode design for nonlinear dynamic systems," *IEEE Trans. Circuit Syst. I*, vol. 49, no. 2, pp. 261–264, Feb. 2002.

Bo Wang (S'16) was born in Shandong, China, in 1987. He received the B.S. degree in electrical engineering from Northwestern Polytechnical University, Xi'an, China, in 2011, and the M.S. degree in electrical engineering in 2013 from Harbin Institute of Technology, Harbin, China, where he is currently working toward the Ph.D. degree in electrical engineering.

His research interests include induction machine drives and nonlinear control theories and applications.

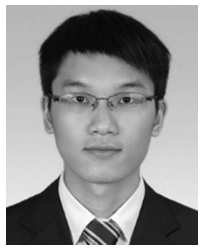

Cheng Luo was born in Hubei, China, in 1991. He received the B.S. degree in water conservancy and hydropower engineering and the M.S. degree in electrical engineering from Huazhong University of Science and Technology, Wuhan, China, in 2014 and 2017, respectively. He is currently working toward the Ph.D. degree in electrical engineering in Harbin Institute of Technology.

His research interests include induction machine drives and parameter identification.

Yong Yu was born in Jilin, China, in 1974. He received the B.S. degree in electromagnetic measurement and instrumentation from the Harbin Institute of Technology (HIT), Harbin, China, and the M.S. and Ph.D. degrees in electrical engineering from HIT, in 1997 and 2003, respectively.

From 2004 to 2014, he was an Associate Professor in the Department of Electrical Engineering, HIT, where he has been a Professor of Electrical Engineering since 2014. His current research interests include electrical motor drives, power quality mitigation, and fault diagnosis and tolerant control of inverter.

Gaolin Wang (M'13) received the B.S., M.S., and Ph.D. degrees in electrical engineering from the Harbin Institute of Technology, Harbin, China, in 2002, 2004, and 2008, respectively.

In 2009, he joined the Department of Electrical Engineering, Harbin Institute of Technology, as a Lecturer, where he has also been a Professor of Electrical Engineering since 2014. From 2009 to 2012, he was a Postdoctoral Fellow in Shanghai STEP Electric Corporation. He has authored more than 30 technical papers published in journals and conference proceedings. He is the holder of seven Chinese patents. His current major research interests include permanent magnet synchronous motor drives, high-performance direct-drive for traction system, position sensorless control of ac motors, and efficiency optimization control of interior PMSM.

Dianguo Xu (M'97–SM'12–F'16) received the B.S. degree in control engineering from Harbin Engineering University, Harbin, China, in 1982, and the M.S. and Ph.D. degrees in electrical engineering from the Harbin Institute of Technology (HIT), Harbin, China, in 1984 and 1989, respectively.

In 1984, he joined the Department of Electrical Engineering, HIT, as an Assistant Professor. Since 1994, he has been a Professor in the Department of Electrical Engineering, HIT. He was the Dean of School of Electrical Engineering and Automation, HIT, from 2000 to 2010. He is currently the Vice President of HIT. His research interests include renewable energy generation technology, power quality mitigation, sensorless vector controlled motor drives, high-performance PMSM servo system. He has published more than 600 technical papers.

Dr. Xu is an Associate Editor of the IEEE TRANSACTIONS ON INDUSTRIAL ELECTRONICS and the IEEE JOURNAL OF EMERGING AND SELECTED TOPICS IN POWER ELECTRONICS. He serves as the Chairman of the IEEE Harbin Section.